The Astrophysical Journal Letters, 873:L20 (6pp), 2019 March 10 https://doi.org/10.3847/2041-8213/ab0c95

Particle-in-cell Simulations of Firehose Instability Driven by Bi-Kappa Electrons

R. A. López[1], M. Lazar[1,2], S. M. Shaaban[1,3], S. Poedts[1], P. H. Yoon[4,5,6], A. F. Viñas[7,8,9], and P. S. Moya[10]
[1] Centre for mathematical Plasma Astrophysics, KU Leuven, Celestijnenlaan 200B, B-3001 Leuven, Belgium; rlopez186@gmail.com
[2] Institut für Theoretische Physik, Lehrstuhl IV: Weltraum- und Astrophysik, Ruhr-Universitt Bochum, D-44780 Bochum, Germany
[3] Theoretical Physics Research Group, Physics Department, Faculty of Science, Mansoura University, 35516, Mansoura, Egypt
[4] Institute for Physical Science and Technology, University of Maryland, College Park, MD, USA
[5] School of Space Research, Kyung Hee University, Republic of Korea
[6] Korea Astronomy and Space Science Institute, Daejeon 34055, Republic of Korea
[7] NASA/Goddard Space Flight Center, Greenbelt, MD 20770, USA
[8] Department of Physics, 200 Hannan Hall, Catholic University of America, Washington, DC 20064, USA
[9] Department of Physics, American University, Washington, DC 20016, USA
[10] Departamento de Física, Facultad de Ciencias, Universidad de Chile, Santiago, Chile
Received 2019 February 1; revised 2019 March 1; accepted 2019 March 5; published 2019 March 15

Abstract

We report the first results from particle-in-cell simulations of the fast-growing aperiodic electron firehose instability driven by the anisotropic bi-Kappa distributed electrons. Such electrons characterize space plasmas, e.g., solar wind and planetary magnetospheres. Predictions made by the linear theory for full wave-frequency and wave-vector spectra of instabilities are confirmed by the simulations showing that only the aperiodic branch develops at oblique angles with respect to the magnetic field direction. Angles corresponding to the peak magnetic field fluctuating power spectrum increase with the increase in the anisotropy and with the decrease in the inverse power-law index κ. The instability saturation and later nonlinear evolutions are also dominated by the oblique fluctuations, which are enhanced by the suprathermals and trigger a faster relaxation of the anisotropic electrons. Diffusion in velocity space is stimulated by the growing fluctuations, which scatter the electrons, starting with the more energetic suprathermal populations, as appears already before the saturation. After saturation the fluctuating magnetic field power shows decay patterns in the wave-vector space and a shift toward lower angles of propagation.

Key words: instabilities – methods: numerical – plasmas – radiation mechanisms: non-thermal – radiation mechanisms: thermal – waves

1. Introduction

Solar wind plasma is sufficiently dilute and therefore highly susceptible to large deviations from isotropy and thermal equilibrium. Particularly relevant are the velocity (or energy) distributions of solar wind electrons, which reveal two central components, a nearly Maxwellian quasithermal core at low energies and a suprathermal halo population at high energies (Maksimovic et al. 2005; Štverák et al. 2008; Pierrard & Lazar 2010). Additional strahls or beaming electrons may also be observed increasing in intensity during fast winds and inducing an additional free energy in the magnetic field direction. In the present work we consider only the central components of the observed distributions, which overall are well described by the (bi-)Kappa distribution functions, as power-law generalizations of the more idealized (bi-)Maxwellian model. Another relevant factor is the free energy of the solar wind expanding along the interplanetary magnetic field, which is expected to accumulate in a temperature anisotropy of protons (ions) $T_\parallel > T_\perp$, where $\parallel$ and $\perp$ denote directions relative to the magnetic field (Chew et al. 1956). For electrons the situation is slightly different, although their temperature anisotropy shows the same tendency, i.e., $T_\parallel > T_\perp$, with increasing the distance from the Sun, see Figure 8 in Štverák et al. (2008; the average behavior of the temperature anisotropy can be found in Adrian et al. 2016). However, the anisotropy reported by the observations at large enough heliocentric distances, e.g., 1 au, is much below these expectation (Adrian et al. 2016; Chen et al. 2016). Looking for an explanation, one can find that particle–particle collisions are inefficient at large distances from the Sun, but the resulting firehose instabilities may constrain the increase of temperature anisotropy in this case. Such a presumption is supported by a reasonable fit of the instability thresholds derived from a bi-Maxwellian plasma approach with the anisotropy limits of the core plasma populations in the solar wind (Štverák et al. 2008). However, the most quasi-stable states restrain to even lower anisotropies, suggesting that these thresholds are underestimated.

A realistic approach should indeed take into account the suprathermal (bi-)Kappa distributed populations of electrons, which are ubiquitous in space plasmas (Maksimovic et al. 2005; Štverák et al. 2008). Recent studies have shown that these populations induce an additional free energy that may significantly stimulate the firehose instabilities (Lazar et al. 2017a, 2017b; Shaaban et al. 2019), of which only the aperiodic branch seems to be much faster and therefore more efficient than the periodic firehose (Shaaban et al. 2019). Indeed, linear theory predicts two branches of electron firehose (EFH) instability for both cases of bi-Maxwellian or bi-Kappa distributed electrons: a left-handed circularly polarized mode, which here is called the periodic EFH (P-EFH) instability (i.e., with a finite wave-frequency $\omega \neq 0$) and may develop along the magnetic field direction and at small angles ($\boldsymbol{k} \cdot \boldsymbol{B} \simeq kB$) (Lazar & Poedts 2009; Viñas et al. 2015, 2017; Lazar et al. 2017b), and another aperiodic EFH (A-EFH) instability propagating only at large (highly oblique) angles, i.e., $\boldsymbol{k} \times \boldsymbol{B} \neq 0$, and growing in time with rates much higher than the P-EFH branch (Li & Habbal 2000; Maneva et al. 2016; Shaaban et al. 2019). These results suggest that only the

A-EFH instability will develop first, consuming part of the free energy and leading to enhanced fluctuations that may scatter the particles and reduce the anisotropy of the distribution.

Indeed, particle-in-cell (PIC) simulations confirm these predictions for an idealized (bi-)Maxwellian plasma (Gary & Nishimura 2003; Camporeale & Burgess 2008; Hellinger et al. 2014; Riquelme et al. 2018), but the effect of suprathermal electrons, ubiquitous in space plasmas, and well described by the bi-Kappa distribution functions—see the review by Pierrard & Lazar (2010)—is not quantified yet. Numerical simulations may offer a complete and dynamical picture providing valuable insights from both the linear and nonlinear phases of the relaxation, to resolve the interplay of kinetic instabilities that may develop for the same plasma conditions and to decode the role played by different populations, in our case the suprathermal electrons. For bi-Kappa distributed plasmas, a theoretical characterization of the whole wave-vector spectrum of kinetic instabilities is complicated even in a linear limit (Summers & Thorne 1991; Summers et al. 1994; Astfalk et al. 2015; Gaelzer & Ziebell 2016; Gaelzer et al. 2016; Kim et al. 2017, 2018; Meneses et al. 2018; Shaaban et al. 2019), and a quasilinear approach is even less straightforward. Here we use particle-in-cell (PIC) simulations and seek to provide answers to these questions from linear and extended quasilinear and nonlinear evolution of the firehose instabilities driven by the bi-Kappa distributed electrons. In particular, the effects introduced by the suprathermal electrons are outlined from a direct comparison with the simulations of bi-Maxwellian electrons of similar anisotropy.

2. Insights from Theory

The anisotropic electrons are assumed to be bi-Kappa distributed (Lazar et al. 2017b)

$$f_\kappa(\boldsymbol{v}) = \frac{n_0 c_\kappa}{\pi^{3/2}\alpha_\perp^2\alpha_\parallel}\left[1+\frac{v_\parallel^2}{\kappa\alpha_\parallel^2}+\frac{v_\perp^2}{\kappa\alpha_\perp^2}\right]^{-\kappa-1}, \quad (1)$$

with $c_\kappa = \Gamma(\kappa)/(\kappa^{1/2}\Gamma(\kappa-0.5))$, and $\alpha_{\parallel,\perp} = (2k_B T_{\parallel,\perp}/m_e)^{1/2}$ are the components of the most probable speed (Vasyliunas 1968), related to the corresponding components of (kinetic) temperature, $T^\kappa_{\parallel,\perp} = \kappa/(\kappa-1.5)T_{\parallel,\perp}$ defined for $\kappa > 1.5$. $\parallel$ and $\perp$ denote directions parallel and perpendicular to the background magnetic field, respectively, and $T = \lim_{\kappa\to\infty} T^\kappa < T^\kappa$ is the temperature of thermal electrons in the Maxwellian core of the observed distribution (Lazar et al. 2015). We study the evolution of the EFH instability assuming the following initial conditions, suggested by the observations in the solar wind at 1 au: $\kappa = 3$ for the inverse power-law index, $T^\kappa_\perp/T^\kappa_\parallel = T_\perp/T_\parallel = 0.2$ for the temperature anisotropy of electrons, $\omega_{pe}/\Omega_{ce} = 100$ for the plasma-to-gyro frequency ratio, and $\beta^\kappa_\parallel = 8\pi n_0 k_B T^\kappa_\parallel/B^2 = 8.0$ for the plasma beta parameter. Thus, the effects of suprathermal electrons can be extracted from a direct contrast with standard results for bi-Maxwellian (quasithermal) electrons in the limit of large $\kappa\to\infty$, implying a lower $\beta_\parallel = 8\pi n_0 k_B T_\parallel/B^2 = 4.0$ (Lazar et al. 2015; Viñas et al. 2015). Protons are considered isotropic and Maxwellian distributed and initially with $\beta_p = 4.0$, for all cases.

We have developed a numerical solver capable of resolving the linear kinetic dispersion and stability properties of such a plasma system. This solver is an extension of the code developed for Maxwellian plasmas (López et al. 2017), but in the present case the integrals in the dispersion tensor are computed by an adaptive numerical quadrature. The components of the dielectric response tensor for (bi-)Kappa plasmas are already presented in the literature, e.g., Gaelzer & Ziebell (2016), Gaelzer et al. (2016), Kim et al. (2017), and Shaaban et al. (2018a) and we do not reproduce them here, but our code is based on the definitions presented by Kim et al. (2017). In Figure 1 we show the variation of the maximum growth rate for both modes, A-EFH (solid lines) and P-EFH (dashed lines), as a function of the angle of propagation θ, for $\kappa = 3$ (red) and $\kappa = \infty$ (black), with $\beta^\kappa_\parallel = 8.0$ and $\beta_\parallel = 4.0$, respectively. For this set of parameters P-EFH dominates over the A-EFH instability only for small angles θ (quasi-parallel propagation), but A-EFH shows much higher peaks of maximum growth rates corresponding to the fastest developing modes; this is much higher than those of the P-EFH branch, which is not expected to play an important role in the linear stage. This peak of A-EFH instability increases in the presence of the suprathermal electrons, and shifts toward higher angles θ. Thus, in Maxwellian limit the A-EFH instability becomes operative at about $\theta \approx 25°$ and growth rates reach a peak for $\theta \approx 77°$, while for $\kappa = 3$ the instability arises near $\theta \approx 40°$ and shows a peak for $\theta \approx 82°$. The influence of suprathermals determines higher (maximum) growth rates for highly oblique angles, i.e., $\theta > 65°$, and a peak almost 1.5 times higher than the Maxwellian one. We also note that suprathermals may induce conditions for the instability of ordinary (O-) mode, marked with a blue cross at exactly $\theta = 90°$.

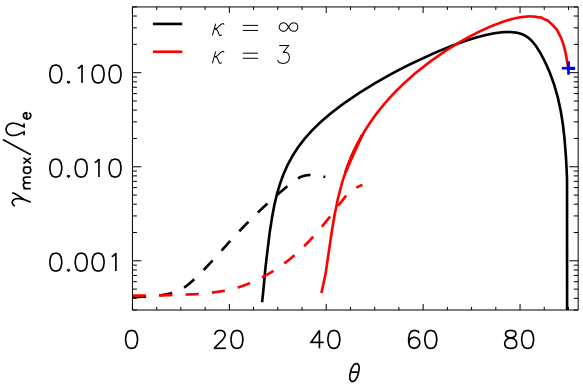

Figure 1. Maximum growth rate γ_{max}/Ω_e as a function of the propagation angle θ for A-EFH (solid) and P-EFH (dashed) branches of EFH instability, for $\kappa = 3$ (red) and Maxwellian limit $\kappa\to\infty$ (black). Blue cross indicate the O-mode at $\theta = 90°$.

Given these preliminary results, in Figure 2 with color levels we plot in more detail only the growth rate for the purely growing A-EFH instability. We use k_x for parallel ($\parallel$) direction and k_y representative for perpendicular $\perp$ plane, in preparation for a comparison with the simulation results in the next section. For $\kappa = 3$ (top panel) the maximum growth rate $\gamma_m/\Omega_e \approx 0.39$ is obtained around $\theta \approx 82°$ $((ck_x/\omega_{pe}, ck_y/\omega_{pe}) \approx (0.13, 1.0))$, while for the Maxwellian limit (bottom panel) maximum growth rate $\gamma_m/\Omega_e \approx 0.27$ is located at $\theta \approx 77°$ $((ck_x/\omega_{pe}, ck_y/\omega_{pe}) \approx (0.22, 1.0))$. Suprathermals enhance the effect of the EFH instability, leading to higher maximum growth rates as the value of κ decreases. It is also obvious that this peak shifts to larger angles as κ decreases, but this shift is not significant. These results are consistent with the recent

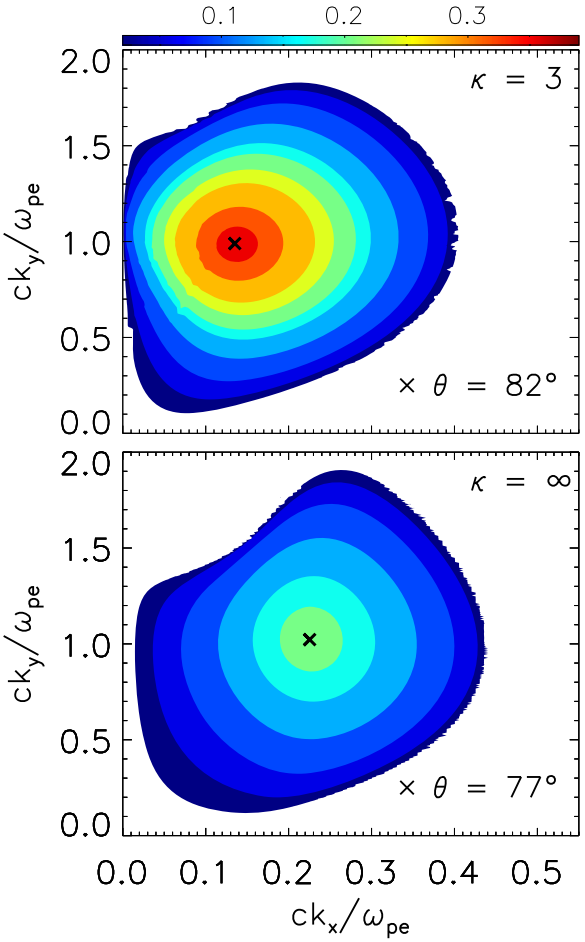

Figure 2. A-EFH growth rate, γ/Ω_e, obtained from the linear dispersion relation in the k_x–k_y plane for $\kappa = 3$ (top) and Maxwellian limit $\kappa \to \infty$ (bottom).

findings of Shaaban et al. (2019) obtained with a different dispersion solver called DSHARK (Astfalk et al. 2015).

3. PIC Simulations

We ran a series of simulations using an explicit 2D PIC code, adapted from the KEMPO1 code of Matsumoto & Omura (1993). The simulation setup is as follows: the spatial grid is composed of $n_x \times n_y = 1024 \times 1024$ cells, with 625 particles per species per grid, with a total of 655.36×10^6 particles per species. We compensate the low number of particles per grid cell by using a quadratic spline interpolation as shape function, requiring nine neighbor cells to compute the charge and current densities (Birdsall & Langdon 1991). The cell width is $\Delta x = \Delta y = 0.2\, c/\omega_{pe}$, so $L_x = L_y = 204.8\, c/\omega_{pe}$. The mass ratio is $m_p/m_e = 1836$, and the plasma-to-gyro frequency ratio for electrons is $\omega_{pe}/\Omega_{ce} = 20$. The background magnetic field is set in the x direction, $\boldsymbol{B}_0 = B_0\hat{\boldsymbol{x}}$. The time step is $\Delta t = 0.01/\omega_{pe}$ and the simulations ran until $t_{\max} = 1310.72/\omega_{pe}$ or equivalently $t_{\max} = 65.536/\Omega_e$. We have chosen a reduced value for the plasma-to-gyro radio, $\omega_{pe}/\Omega_e = 20$, in order to save computational resources. Although the growth rates in Figure 2 are calculated for $\omega_{pe}/\Omega_e = 100$, the dispersion relation depends very weakly on this ratio, and the results are practically identical (not shown).

The free energy available in the initially anisotropic distribution is then relaxed by the excitation of the EFH

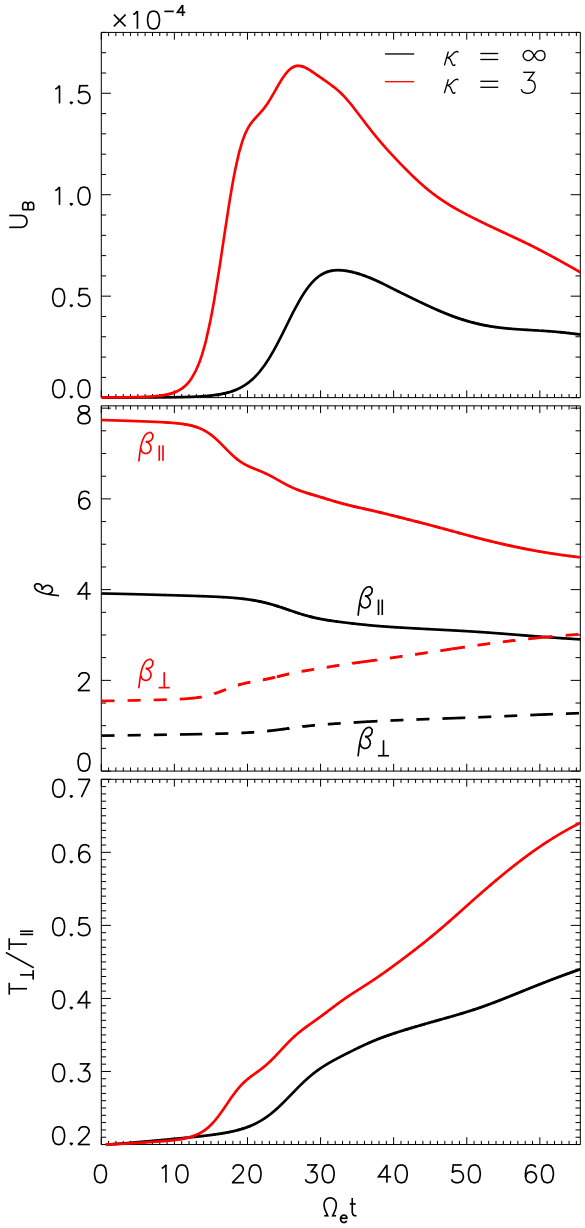

Figure 3. Time evolution of the fluctuating magnetic energy density (top panel), the parallel and perpendicular electron plasma betas (middle panel), and electron temperature anisotropy (bottom panel) for $\kappa = 3$ (red) and Maxwellian (black).

instability. In Figure 3 (top panel) we show the evolution of the fluctuating magnetic energy density, U_B, for the whole time interval of the simulation. The solid red line is obtained in the presence of suprathermal electrons ($\kappa = 3$), while the solid black line is derived in the Maxwellian limit ($\kappa \to \infty$). Suprathermal electrons have an important effect in the evolution of the instability, as we observe that the magnetic field energy density reaches a maximum level almost three times higher. The instability develops also faster as the slope of the exponentially growing magnetic field energy density becomes steeper for low values of κ, which is consistent with the fact that the growth rates obtained in Figure 2 are much higher than those obtained for Maxwellian electrons. Suprathermal electrons reach the saturation stage over a shorter time period, magnetic field energy density reaching maximum

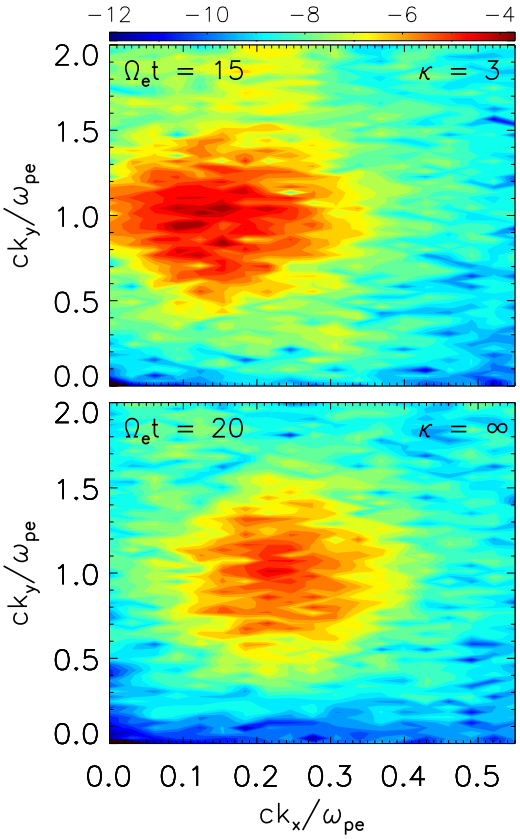

Figure 4. Snapshot of δB_z spectral power from the linear growing phase in the simulations for $\kappa = 3$ (top panel) and Maxwellian (bottom panel).

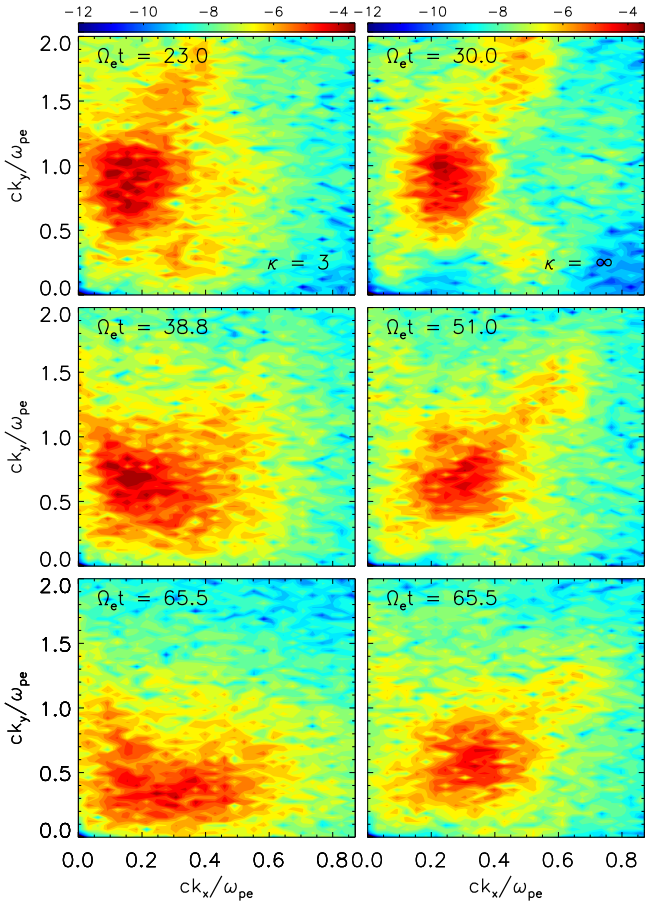

Figure 5. δB_z spectral power from relevant moments in the simulation, for $\kappa = 3$ (left panels) and Maxwellian (right panels).

intensity around $t_{\rm sat} \approx 27/\Omega_e$, while for Maxwellian electrons the corresponding saturation time is $t_{\rm sat} \approx 32/\Omega_e$.

The middle panel in Figure 3 shows the evolution of parallel and perpendicular plasma betas, for both the bi-Maxwellian and bi-Kappa distributed electrons. All cases show the typical effects of the firehose instability, namely, a reduction in the parallel plasma beta at expenses of an increase in the perpendicular plasma beta, resulting in the relaxation of the anisotropic electrons, as shown in the bottom panel in Figure 3. Notice a much faster reduction of the anisotropy (i.e., deviation from isotropy) in the presence of suprathermal electrons. In the very early stage of the evolution, $0 < \Omega_e t < 12$ for $\kappa = 3$ and $0 < \omega_e t < 18$ for Maxwellian, these quantities show very little changes, as the fluctuating amplitudes are still too low to affect the electron distribution. This time stage is mainly dominated by the spontaneous fluctuations randomly generated by the thermal motion of charged particles that act as the seed perturbation triggering the instability. The level of these fluctuations is directly related to the number of particles used in the simulation (López & Yoon 2018). Simulations with low number of particles per grid cell introduce large statistical fluctuations in the charge and current densities, which results in a high level of numerical noise. That noise can be amplified by the electromagnetic instabilities, accelerating the growth of the fluctuations (see Figure 2 in López & Yoon 2018).

In Figure 4 we plot the spectral power (logarithmic scale) of the dominant fluctuating magnetic field component, δB_z, in the k_x–k_y plane, at the early stage of the instability growth, $\Omega_e t = 15$ for $\kappa = 3$ and $\Omega_e t = 20$ for Maxwellian. A direct comparison of Figures 2 and 4 shows a very good agreement between linear theory and simulations. The instability is enhanced by the suprathermal electrons and covers a wider range of wave numbers, including very large angles (low k_x). Simulations also confirm the excitation of the Ordinary (O-) mode fluctuations at $\theta = 90^\circ$ ($k_x = 0$) in the presence of suprathermals, as already suggested by the linear growth rates in Figures 1 and 2. The evolution of the spectral power in the wave-vector space is showed in Figure 5, left panels for $\kappa = 3$ and right panels for Maxwellian. We show three different snapshots, close to but right before the saturation of the instability (top panels), after the saturation (middle panels), and at the end of the simulation (bottom panels). After the instability saturation the maximum fluctuating power shifts toward lower angles of propagation (with respect to the magnetic field), as also previously reported for bi-Maxwellian electrons (Camporeale & Burgess 2008). This also increases the range of unstable wave numbers, i.e., x direction, possibly from nonlinear decays of the large amplitude fluctuations.

The reduced electron velocity distribution function in a 2D velocity space, e.g., $f(v_x, v_y)$, as defined, respectively, by the parallel and perpendicular directions, is shown in Figure 6 for three different time intervals during the simulations: initial conditions (top panels) of the simulations starting either from a bi-Kappa (left, $\kappa = 3$) or from a bi-Maxwellian (right), shortly before the saturation (middle panels) and after the saturation of the instability (bottom panels). The lowest level plotted corresponds to $10^{-3} f_{\rm max}$. Evolution of the Maxwellian electrons is consistent with previous results, shown for instance in Hellinger et al. (2014). The effect of instability is to reduce the

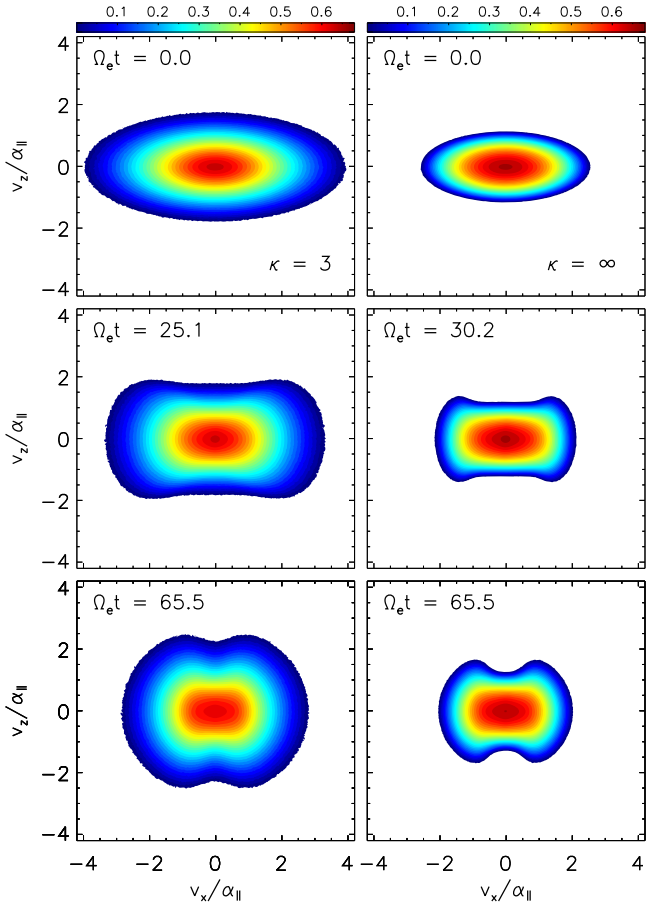

Figure 6. Electron velocity distribution function in the v_x–v_z space from relevant moments in the simulation, for $\kappa = 3$ (left panels) and Maxwellian (right panels).

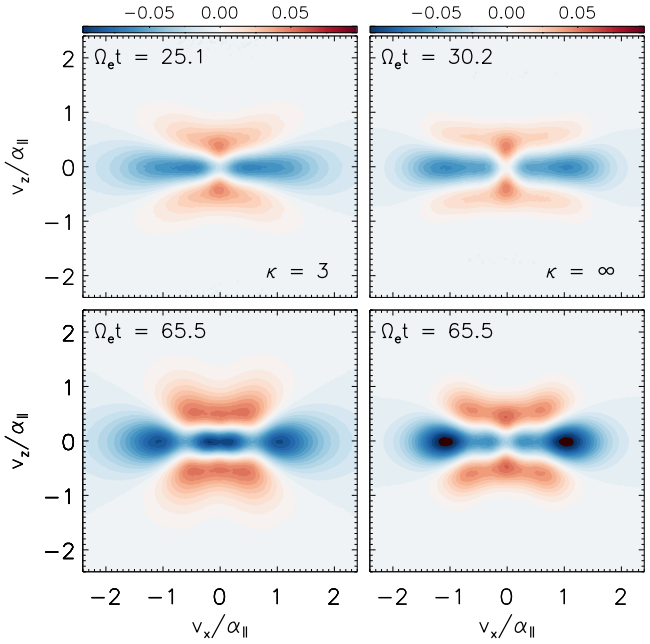

Figure 7. Snapshots of the electron velocity distributions $\delta f = f(t) - f(0)$ for $\kappa = 3$ (left panels) and Maxwellian (right panels).

effective anisotropy in both cases, $\kappa = 3$ and Maxwellian ($\kappa \to \infty$). Suprathermal (high-energy) populations show a more pronounced tendency of isotropization, and, according to trends in Figure 3, this should continue in time (not shown here) to explain the low limits of temperature anisotropy reported by the observations for the quasi-stable states of electrons in space plasmas, e.g., in Štverák et al. (2008).

Energetic suprathermal electrons are rapidly scattered by the enhanced fluctuations that trigger their diffusion in velocity space, leading to a fast redistribution in perpendicular direction, and implicitly to a lower anisotropy. Finally, in Figure 7 we plot $\delta f = f(t) - f(0)$ in order to quantify these variations in the time evolution of the velocity distributions. Blue indicates negative values, i.e., a reduction in the distribution, and red shows positive values, i.e., an increase of the populations, which helps us to visualize and quantify the electron diffusion from parallel to perpendicular direction. This region is more negative, i.e., darker blue, for a Maxwellian that is less populated at high energies. After the saturation of the instability a secondary electron-depleted region appears, also in parallel direction, proving that the intense fluctuations are able to scatter the more dense and less energetic electrons from the core.

4. Conclusions

In this Letter we have carried out a detailed study of the EFH instability, first by employing the linear stability analysis for both bi-Maxwellian distributed electrons and for suprathermal electrons modeled by bi-Kappa distribution. We have then carried out a 2D PIC code simulation in order to investigate the nonlinear phase of the instability. It is found that for both bi-Maxwellian and bi-Kappa suprathermal electrons, the A-EFH has a much higher maximum growth rate when compared with the P-EFH branch, which confirms earlier findings. We found that the bi-Kappa suprathermal electrons are more unstable to the firehose mode excitation when compared with the bi-Maxwellian case, which is shown in both linear analysis and subsequent long-running simulations.

In the simulations the saturation of instability is faster, and the wave magnetic field intensity reaches higher amplitude in the presence of suprathermal electrons. The corresponding temperature relaxation, perpendicular heating, and parallel cooling also exhibit a consistent trend in that the bi-Kappa suprathermal electron runs produce more noticeable dynamical changes. The investigation of 2D spectral properties associated with the time-evolving instability shows that the firehose instability progressively takes on the field-aligned, or parallel characteristics, thus obliquity is being reduced. This trend is common to both bi-Kappa and bi-Maxwellian electrons. The particle distribution function exhibits appreciable departure from the initial bi-Kappa or bi-Maxwellian characteristics in that the pitch angle scattering (or diffusion), which primarily affects the high-velocity populations of electrons, leads to a significant deformation of the initial velocity distribution function such that as time progresses, the velocity space contours resemble a dumbbell shape. We have also analyzed the nature of wave-particle interaction by plotting the perturbed distribution function, and identified the region of velocity space, which leads to the enhanced versus depressed phase space distribution function. Such a plot helps to understand the cause of the deviation of simulated velocity distribution functions from their initial configurations.

The significance of the present findings in the context of space and astrophysical plasmas is that the relaxation of temperature anisotropy in the electrons by the aperiodic, or oblique, firehose instability is shown to be dominant over the parallel counterpart.

In the literature, large-scale solar wind models combined with kinetic-scale physics attempted to include the relaxation of excessive electron temperature anisotropy by parallel firehose instability within the quasilinear model (Sarfraz et al. 2017; Yoon & Sarfraz 2017; Yoon et al. 2017; Sarfraz 2018; Shaaban et al. 2019). However, the present theory and simulation study shows that it is imperative to include the influence of oblique firehose instability, as such an unstable mode is expected to dominate the electron dynamics. Thus, the present work poses a challenge for the modelers of large-scale solar wind that integrate kinetic-scale physics in that, the future more complete models should incorporate the oblique firehose instability calculation in the quasilinear analysis.

It is also worth mentioning that in the present work we have neglected the presence of the strahl or beaming electrons, which may be relevant in the fast solar winds. Strahl population introduces effective free energy in the parallel direction, and can markedly change the dispersion properties leading to more complex instabilities, e.g., heat-flux instability from the interplay of strahls with temperature anisotropies (Shaaban et al. 2018b). Our present results should stimulate future numerical studies to integrate the strahl component and provide a complete picture of the instability conditions in this case.

These results were obtained in the framework of the projects SCHL 201/35-1 (DFG-German Research Foundation), GOA/2015-014 (KU Leuven), G0A2316N (FWO-Vlaanderen), and C 90347 (ESA Prodex 9). S.M.S. acknowledges support by a FWO Postdoctoral Fellowship (grant No. 12Z6218N). P.H.Y. acknowledge BK21 Plus program from NRF (Korea). A.F.V. thanks the NASA/MMS Guest Investigation Program for their support. We also appreciate the support from the International Space Science Institute (ISSI) for hosting the international ISSI team on Kappa Distributions, which triggered fruitful discussions that were beneficial for the work presented here.

ORCID iDs

R. A. López https://orcid.org/0000-0003-3223-1498
M. Lazar https://orcid.org/0000-0002-8508-5466
S. M. Shaaban https://orcid.org/0000-0003-0465-598X
S. Poedts https://orcid.org/0000-0002-1743-0651
P. H. Yoon https://orcid.org/0000-0001-8134-3790
A. F. Viñas https://orcid.org/0000-0001-5912-5703
P. S. Moya https://orcid.org/0000-0002-9161-0888

References

Adrian, M. L., Viñas, A. F., Moya, P. S., & Wendel, D. E. 2016, ApJ, 833, 49
Astfalk, P., Görler, T., & Jenko, F. 2015, JGRA, 120, 7107
Birdsall, C. K., & Langdon, A. B. 1991, Plasma Physics via Computer Simulation (Bristol: Hilger)
Camporeale, E., & Burgess, D. 2008, JGRA, 113, A07107
Chen, C. H. K., Matteini, L., Schekochihin, A. A., et al. 2016, ApJL, 825, L26
Chew, G. F., Goldberger, M. L., & Low, F. E. 1956, RSPSA, 236, 112
Gaelzer, R., & Ziebell, L. F. 2016, PhPl, 23, 022110
Gaelzer, R., Ziebell, L. F., & Meneses, A. R. 2016, PhPl, 23, 062108
Gary, S. P., & Nishimura, K. 2003, PhPl, 10, 3571
Hellinger, P., Trávníček, P. M., Decyk, V. K., & Schriver, D. 2014, JGRA, 119, 59
Kim, S., Lazar, M., Schlickeiser, R., López, R. A., & Yoon, P. H. 2018, PPCF, 60, 075010
Kim, S., Schlickeiser, R., Yoon, P. H., López, R. A., & Lazar, M. 2017, PPCF, 59, 125003
Lazar, M., Pierrard, V., Shaaban, S., Fichtner, H., & Poedts, S. 2017a, A&A, 602, A44
Lazar, M., & Poedts, S. 2009, A&A, 494, 311
Lazar, M., Poedts, S., & Fichtner, H. 2015, A&A, 582, A124
Lazar, M., Shaaban, S. M., Poedts, S., & Štverák, Š. 2017b, MNRAS, 464, 564
Li, X., & Habbal, S. R. 2000, JGRA, 105, 27377
López, R. A., Viñas, A. F., Araneda, J. A., & Yoon, P. H. 2017, ApJ, 845, 60
López, R. A., & Yoon, P. H. 2018, JGRA, 123, 8924
Maksimovic, M., Zouganelis, I., Chaufray, J.-Y., et al. 2005, JGRA, 110, A09104
Maneva, Y., Lazar, M., Viñas, A., & Poedts, S. 2016, ApJ, 832, 64
Matsumoto, H., & Omura, Y. (ed.) 1993, Computer Space Plasma Physics: Simulation Techniques and Software (Tokyo: Terra Scientific Publishing Company)
Meneses, A. R., Gaelzer, R., & Ziebell, L. F. 2018, PhPl, 25, 112901
Pierrard, V., & Lazar, M. 2010, SoPh, 267, 153
Riquelme, M., Quataert, E., & Verscharen, D. 2018, ApJ, 854, 132
Sarfraz, M. 2018, JGRA, 123, 6107
Sarfraz, M., Yoon, P. H., Saeed, S., Abbas, G., & Shah, H. A. 2017, PhPl, 24, 012907
Shaaban, S. M., Lazar, M., Astfalk, P., & Poedts, S. 2018a, JGRA, 123, 1754
Shaaban, S. M., Lazar, M., López, R. A., Fichtner, H., & Poedts, S. 2019, MNRAS, 483, 5642
Shaaban, S. M., Lazar, M., Yoon, P. H., & Poedts, S. 2018b, PhPl, 25, 082105
Shaaban, S. M., Lazar, M., Yoon, P. H., & Poedts, S. 2019, ApJ, 871, 237
Summers, D., & Thorne, R. M. 1991, PhFlB, 3, 1835
Summers, D., Xue, S., & Thorne, R. M. 1994, PhPl, 1, 2012
Štverák, Š., Trávníček, P., Maksimovic, M., et al. 2008, JGRA, 113, A03103
Vasyliunas, V. M. 1968, JGRA, 73, 2839
Viñas, A. F., Gaelzer, R., Moya, P. S., Mace, R. L., & Araneda, J. A. 2017, in Kappa Distributions, ed. G. Livadiotis (Amsterdam: Elsevier), 329
Viñas, A. F., Moya, P. S., Navarro, R. E., et al. 2015, JGRA, 120, 3307
Yoon, P. H., López, R. A., Seough, J., & Sarfraz, M. 2017, PhPl, 24, 112104
Yoon, P. H., & Sarfraz, M. 2017, ApJ, 835, 246